

Chemical Science

Accepted Manuscript

This article can be cited before page numbers have been issued, to do this please use: B. Du, Y. Lin, J. Ma, W. Gu, F. Liu, Y. Yao and L. Song, *Chem. Sci.*, 2025, DOI: 10.1039/D4SC06932C.



This is an Accepted Manuscript, which has been through the Royal Society of Chemistry peer review process and has been accepted for publication.

Accepted Manuscripts are published online shortly after acceptance, before technical editing, formatting and proof reading. Using this free service, authors can make their results available to the community, in citable form, before we publish the edited article. We will replace this Accepted Manuscript with the edited and formatted Advance Article as soon as it is available.

You can find more information about Accepted Manuscripts in the [Information for Authors](#).

Please note that technical editing may introduce minor changes to the text and/or graphics, which may alter content. The journal's standard [Terms & Conditions](#) and the [Ethical guidelines](#) still apply. In no event shall the Royal Society of Chemistry be held responsible for any errors or omissions in this Accepted Manuscript or any consequences arising from the use of any information it contains.

Buried Interface Management toward High-Performance Perovskite Solar Cells†

Bin Du^{a#*}, Yuexin Lin^{b#}, Jintao Ma^a, Weidan Gu^a, Fei Liu^a, Yijun Yao^{c*}, and Lin Song^{d*}

^a *School of Materials Science and Engineering, Xi'an Polytechnic University, Xi'an 710048, China*

^b *MOE Key Laboratory for Nonequilibrium Synthesis and Modulation of Condensed Matter, School of Physics, National Innovation Platform (Center) for Industry-Education Integration of Energy Storage Technology, Xi'an Jiaotong University, Xi'an 710049, P. R. China*

^c *School of Textile Science and Engineering, Xi'an Polytechnic University, Xi'an, 710048, Shaanxi, China*

^d *Frontiers Science Center for Flexible Electronics (FSCFE), Institute of Flexible Electronics (IFE), Northwestern Polytechnical University, Xi'an 710072, China*

Authors share equal authorship

† Electronic supplementary information (ESI) available.

* dubin@xpu.edu.cn (B. D)

* yaoyj@xpu.edu.cn (Y. Y)

* iamsong@nwpu.edu.cn (L. S)



Abstract

View Article Online
DOI: 10.1039/D4SC06932C

The interface between the perovskite layer and the electron transport layer is an extremely important factor that cannot be ignored in achieving high-performance perovskite photovoltaic technology. However, the void defects of the interface pose a serious challenge for high performance perovskite solar cells (PSCs). To address this, we report a polydentate ligand reinforced chelating strategy to strengthen the stability of buried interface by managing interfacial defects and stress. The gelatin-coupled cellulose (GCC) is employed to manipulate the buried interface. The unique functional groups in GCC synergistically passivate the defects from the surface of SnO₂ and the bottom surface of the perovskite layer. Our work demonstrates that by implementing the GCC as a buried interface strategy, it is possible to prepare devices with reduced vacancy states, non-radiative recombination suppression, and excellent optoelectronic performance. At the same time, this work improves the efficiency and stability of PSCs, and provides greater space for device manufacturing.

Keywords: Perovskite Solar Cells, Buried Interface, Passivate the defects, Gelatin-Coupled Cellulose

1. Introduction

Perovskite solar cells (PSCs) have emerged as a research frontier of photovoltaic technologies with their excellent photovoltaic properties, including long carrier lifetimes, high light absorption coefficients, adjustable band gaps and high defect tolerance.¹⁻⁵ So far, the highest certified power conversion efficiency (PCE) has exceeded 26%.⁶⁻¹⁰ However, long-term stability remains a major bottleneck for commercial application, which requires a product lifetime of approximately 20–25 years.¹¹⁻¹⁵ For typical n-i-p PSCs, the electron transport layer (ETL) is an important component of PSCs, responsible for transporting electrons and blocking holes. How to fabricate high-quality ETLs with reduced defects is the key to achieve efficient and stable n-i-p PSCs.¹⁶⁻¹⁸ The interfaces between adjacent functional layers in PSCs through which photogenerated carriers complete the extraction, transport, and collection processes during the operation of PSCs.¹⁹ The favorable band alignment between the ETL and the perovskite film facilitates charge extraction, charge complex



inhibition and long-term device stability.²⁰ Therefore, the resulting performance of PSCs is closely related to the nature of these interfaces. Due to the inconsistent lattice constants of each functional layer within PSCs, defects at the interface tend to be more numerous than those in perovskite bulk, leading to more severe non-radiative composites.²¹ As one of the most widely used ETL materials in n-i-p PSCs, tin oxide (SnO₂) exhibits various advantages such as high electron mobility and high transmittance, and excellent photo stability. Since the deposition of SnO₂ is prearranged prior to the preparation of perovskite films in n-i-p structured PSCs, it dominates perovskite crystallization and interfacial charge transport.^{22–24} Therefore, high-quality SnO₂ film are crucial for achieving high-performance PSCs. Whereas, generally for the surface of SnO₂ films prepared by sol-gel method, there are a large number of defects (e.g., oxygen and tin vacancies, interstitial and antisite defects), which can lead to charge accumulation and interfacial non-radiative recombination loss, limiting the photovoltaic performance and operational stability of PSCs.^{25,26} In addition, the imperfect band alignment between SnO₂ and perovskite exacerbates the hysteresis-induced charge extraction block. The high efficiency of PSCs is achieved by increasing the charge transfer efficiency between the interfaces and reducing the non-radiative compounding.^{27,28} Interfacial engineering aims to passivate interfacial defects or adjust the band alignment by introducing Interface layers or improving the interfacial properties to reduce losses.^{29,30} Therefore, modification of the SnO₂/perovskite interface has attracted the attention of many researchers as a simple and feasible strategy that can both passivate the interfacial defects efficiently, and connect the perovskite layer and lower functional layers, thus enabling the optimization of perovskite crystals at the same time.^{31–33}

In this work, gelatin-coupled cellulose (GCC) was first used to modify the SnO₂/perovskite interface, which contribute to both interfacial modification and crystalline modulation. The results show that GCC can interact strongly with both SnO₂ and perovskite layers, forming a bridge-like role at the buried interface to achieve the improvement of charge transfer and modulation of the energy level structure. Specifically, strong hydrogen bonds will form between -NH₂/-NH₃⁺ in GCC and I/I⁻ in PbI₂, which can anchor I⁻ on the surface of SnO₂ and promote the uniform growth of PbI₂ and perovskite. On the other hand, the carbonyl groups in GCC can form chemical bonds with uncoordinated Pb²⁺ and reduce the bottom defects of the perovskite layer. In addition, cellulose contains a large number of hydroxyl groups that can coordinate with



the uncoordinated Sn^{4+} in SnO_2 , thereby filling the oxygen vacancies in SnO_2 thin films and passivating the surface defects of SnO_2 . Thus, more matched energy levels can be formed between SnO_2 , GCC and perovskite layers, which will help electron extraction and transport. As a result, compared to the initial device (PCE of 21.68%), the GCC-modified device achieves a significant enhancement of PCE to 25.06%. Moreover, the GCC-modified device maintains 91% of the initial PCE without encapsulation after aging under ambient conditions (25 °C, RH = 20-30%) for more than 1080 h. On the contrary, the control device only retained 70% of its initial PCE. This excellent stability could be attributed to the high crystallinity of perovskite grains and the defect passivation of GCC between SnO_2 and perovskite layers. This work has provided an opportunity to improve the perovskite film's crystal quality, reduce grain boundary and SnO_2 surface defects, modulate the energy level structure of SnO_2 , and improve the electron transfer ability in PSCs provides a feasible and effective interfacial modification strategy, while the combination of interfacial management and energy level control used for embedding opens up new perspectives for achieving high-performance and stable and durable PSCs.

2. Results and Discussion

Cellulose is a biological polymer containing plenty of hydroxyl groups, which can coordinate with uncoordinated Sn^{4+} so that the oxygen vacancy in the SnO_2 film is filled, thereby passivating the surface defects of SnO_2 .^{34,35} In this paper, in order to enhance interfacial contact between SnO_2 and perovskite layer, a modified cellulose, called the GCC, has been synthesized (as shown in Fig. S1.), which introduces a small molecule cinnamyl chloride to react with hydroxyl groups of cellulose,³⁶ aiming to anchor carbonyl groups in the side chain of cellulose. These carbonyl groups could form chemical bonds with uncoordinated Pb^{2+} and reduce the bottom imperfections of perovskite layer.^{37,38} The schematic diagram of mechanism is displayed in Fig. 1.

View Article Online
DOI: 10.1039/D4SC06932C



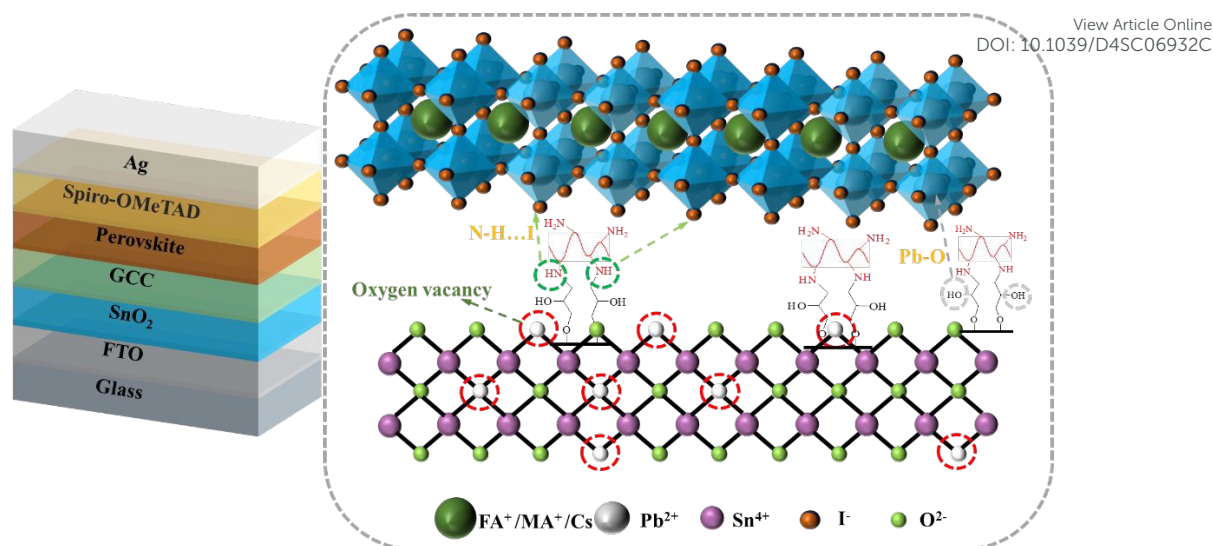


Fig. 1. A schematic diagram of the modification mechanism of GCC at the ETL/perovskite interface is proposed. The chemical structure of the GCC molecule is shown in the middle of the diagram.

To gain a deeper understanding of the mechanism between SnO₂ ETL and GCC, X-ray photoelectron spectroscopy (XPS) measurements were performed (as shown in Fig. S2). As seen from the XPS result in Fig. 2a, the binding energies of Sn 3d_{3/2} (495.54 eV) and Sn 3d_{5/2} (487.13 eV) of SnO₂ were both shifted to higher binding energies of 495.64 and 487.23 eV after modification with GCC, indicating the strong chemical interaction between GCC interlayer and SnO₂, which may result from the coordination between uncoordinated Sn⁴⁺ on the surface of SnO₂ and hydroxyl in GCC molecules. The O 1s XPS spectra are shown in Fig. 2b, c. The O 1s characteristic peaks of the original SnO₂ and SnO₂/GCC films can be convoluted into two sub-peaks which are assigned to the lattice oxygen (O_L) and oxygen vacancies (O_V) in SnO₂, respectively. O_L represents the O²⁻ ions combined with the adjacent metal ions in the lattice, and O_V represents the O²⁻ ions in the O_V region. The O_V content in the film can be estimated by the peak area (R_{OV}) of O_V. The concentrations of O_V and O_L can be represented by the corresponding area of O_V and O_L peaks. The ratio of O_V (R_{OV}) was calculated by the formula: $R_{OV} = S_{OV} / (S_{OV} + S_{OL})$, where S_{OV} and S_{OL} represent the peak area of O_V and O_L, respectively.³⁹ After calculation, R_{OV} was significantly reduced from 0.3495 (pristine SnO₂) to 0.1242 (GCC-treated SnO₂). The decrease in R_{OV} represents the reduction of oxygen vacancies in the SnO₂ film, indicating that GCC can passivate oxygen-deficient defects of SnO₂ films.



To further study the effect of GCC on perovskite layer, XPS measurements are also carried out to analyze perovskite film based on pristine SnO₂ and GCC-modified SnO₂. As shown in the Pb 4f XPS spectrum of Fig. 2d, the perovskite crystal lattice produced two distinct Pb 4f peaks at 138.40 eV and 143.26 eV, which were attributed to Pb 4f_{7/2} and Pb 4f_{5/2}, respectively. After GCC treatment, these two main peaks were shifted to higher binding energies at 138.47 eV and 143.36 eV, respectively, which was attributed to the reduction of electrons around Pb atoms when the carbonyl group in GCC electrostatically coupled with the uncoordinated Pb²⁺. This is due to the reduction of electrons around the Pb atoms when the carbonyl group in the GCC is electrostatically coupled to the uncoordinated Pb²⁺ at the bottom of the perovskite film, which allows the Pb²⁺ defects in the perovskite film to be passivated effectively.⁴⁰ Similarly, the electrons around the Pb atoms in the perovskite films attributed to I 3d_{5/2} and I 3d_{3/2} also increase from the initial 619.22 eV and 630.73 eV to 619.35 eV and 630.88 eV, respectively, as shown in Fig. 2e. This indicates that GCC also strongly interacts with I⁻ in perovskite, which reduces the migration of I⁻ and effectively inhibits the formation of I₂ defects. In addition, the increase in binding energy is due to the fact that I⁻ can provide additional negative charge to fill the O_v through electrostatic coupling, which also verifies the results of the O 1s XPS spectra. The XPS full spectra of SnO₂ and SnO₂/GCC thin films are shown in Fig. 2f. These XPS characterization results confirm that GCC can be used as an interfacial crosslinker to passivate the defects on the surface of SnO₂ films as well as to interact with the bottom of the perovskite layer, which greatly enhances the interfacial contact between the SnO₂ ETL and the perovskite film.

View Article Online
DOI: 10.1039/D4SC06932C



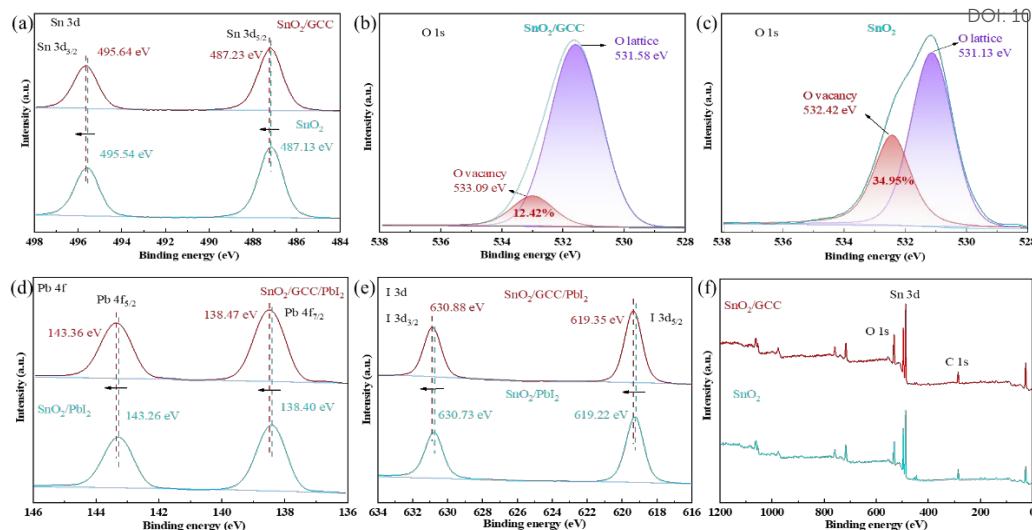


Fig. 2. XPS high-resolution spectra of SnO₂ and SnO₂/GCC for (a) Sn 3d and (b), (c) O 1s. XPS high-resolution spectra of SnO₂/PbI₂ and SnO₂/GCC/PbI₂ for (d) Pb 4f and (e) I 3d. (f) XPS full spectra of SnO₂ and SnO₂/GCC.

We perform ultraviolet photoelectron spectroscopy (UPS) to study the work function (W_F) of SnO₂ films before and after modification to explain the effect of introducing GCC on the interface energy level structure. Fig. 3a show the UPS spectra of SnO₂ and SnO₂/GCC thin films, respectively. The high binding energy edges and low binding energy edges on both sides of the UPS spectrum are referred to as cut-off edge (E_{cutoff}) and Fermi edge ($E_{F, \text{edge}}$), respectively.⁴¹ Fig. 3b,c show the E_{cutoff} and $E_{F, \text{edge}}$ of SnO₂ and SnO₂/GCC thin films characterized by UPS, respectively. The E_{cutoff} of SnO₂ and SnO₂/GCC is 16.61 eV and 16.57 eV, and the $E_{F, \text{edge}}$ is 3.92 eV and 3.73 eV, respectively. Fig. 3d is a Tauc plots converted from relevant UV-Vis spectra, from which the band gaps of SnO₂ and SnO₂/GCC thin films were fitted to be 3.90 eV, indicating that the introduction of GCC did not change the band gap of SnO₂ thin films. Fig. S3 show UPS spectra of SnO₂/Perovskite film. The Fermi levels of different thin films can be calculated using formula.⁴²

$$\begin{cases} -E_{VB} = E_{He(I)} - E_{\text{cutoff}} + E_{F, \text{edge}} \\ E_{CB} = E_{VB} + E_g \end{cases}$$

After calculation, the Fermi level values of SnO₂ and SnO₂/GCC are -4.61 eV and -3.65 eV, respectively. The valence-band energy level (E_{VB}) values are calculated to be -8.53 eV and -8.38 eV, respectively. The conduction-band energy level (E_{CB}) values are -4.63 eV and -4.48 eV, respectively. Therefore, the detailed energy level diagrams of SnO₂ and SnO₂/GCC are shown in Fig. 3e. It can be observed that SnO₂ and SnO₂/GCC



achieve a stepped energy level arrangement, and significant downward band bending occurs at the GCC modified interface. This is beneficial for improving unipolar charge extraction and suppressing interface recombination, promoting electron extraction and transport, and greatly reducing V_{OC} losses in PSCs, improving the electron collection efficiency of PSCs cathode for charge carriers. Table S1 provides detailed parameters of the energy levels of SnO_2 and SnO_2/GCC .

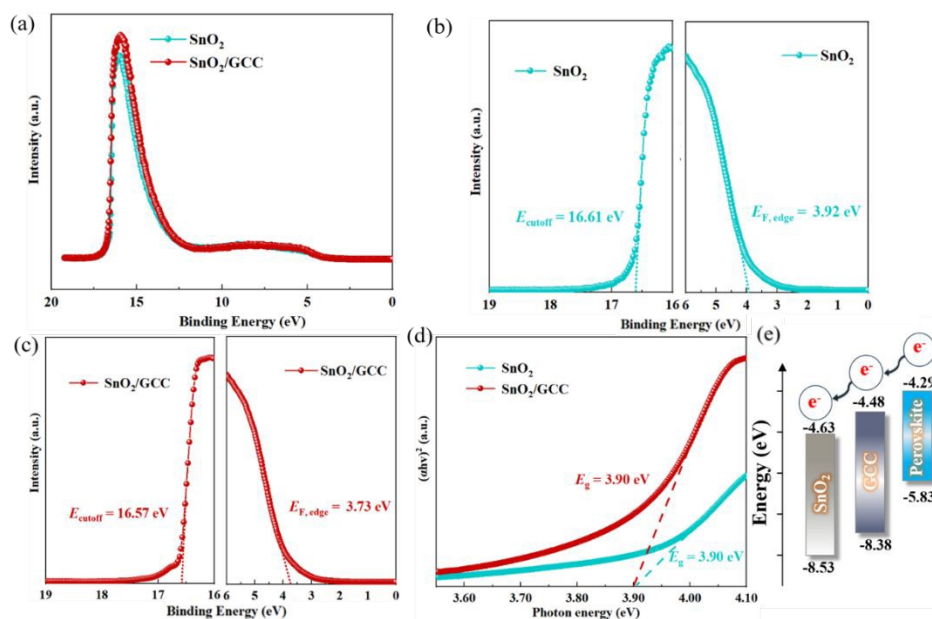


Fig. 3. (a) UPS full spectra of SnO_2 and SnO_2/GCC . UPS spectra of (b) SnO_2 film and (c) SnO_2/GCC film. (d) Tauc-Plot spectra of perovskite films deposited on SnO_2 and SnO_2/GCC substrate. (e) The energy level diagram of SnO_2 , SnO_2/GCC , and perovskite

In order to investigate the effect of GCC interface introduction on the morphology of perovskite films, we characterized the perovskite films deposited on SnO_2 ETL and SnO_2/GCC ETL by optical microscope (OM), scanning electron microscope (SEM) and atomic force microscopy (AFM), respectively, and studied the effect of GCC bridging interlayer on the morphology of the upper perovskite. The OM test results in Fig. S5 indicate that the perovskite film deposited on the control group SnO_2 film has obvious pinholes, while the perovskite film grown on SnO_2/GCC ETL has higher quality and no obvious pinholes. The SEM image in Fig. 4a shows that compared to the original film, the grain size of the perovskite film grown on SnO_2/GCC ETL significantly increases, which may be attributed to the interaction between carbonyl groups and PbI_2 in GCC, resulting in slow crystal growth. Larger grain size and improved morphology facilitate charge transfer and reduce energy loss of PSCs caused by defects. The AFM



image in Fig. 4b shows that the perovskite film formed after GCC modification exhibits a pinhole free morphology, and the root means square (RMS) roughness also decreases from 37.19 nm of the original SnO₂ film to 24.64 nm. In addition, Fig. S4 also illustrates the role of GCC. This result supports the conclusion of SEM measurement, proving that GCC can effectively optimize the morphology of perovskite films and improve film quality. High quality perovskite films are more conducive to reducing electron transport pathways and enhancing carrier transport capabilities. Fig. 4c shows the X-ray diffraction (XRD) patterns of perovskite films grown on different ETL substrates, and the crystallization properties of perovskite films were analyzed through XRD testing. The two typical diffraction peaks at 14.2° and 28.2° that significantly appear in both the original film and the modified film are attributed to the (110) and (220) crystal planes that dominate crystallinity and stability in perovskite, respectively. For GCC modified thin films, the intensity of the (110) and (220) crystal plane peaks are higher, which further indicates that introducing GCC on SnO₂ can promote the crystal growth of perovskite. This result is consistent with the results of SEM and AFM images.

In order to further investigate the crystal structure and orientation of GCC modified perovskite films, we performed the grazing incidence angle wide-angle X-ray scattering (GIWAXS) test of perovskite films deposited on different ETL substrates in different dimensions (Fig. 4d,e). From the two-dimensional (2D) image in Fig. 4d, it can be seen that the SnO₂/GCC ETL based perovskite film exhibits a typical three-dimensional (3D) perovskite structure. Typical scattering rings corresponding to the (110) and (220) crystal planes of perovskite can be clearly observed at $q \approx 1 \text{ \AA}^{-1}$ and $q \approx 2 \text{ \AA}^{-1}$. Then, we conducted one-dimensional (1D) integration analysis on the 2D diffraction pattern around the perovskite (110) crystal plane to more clearly quantify the difference in crystallinity of the film before and after modification, as shown in Fig. 4e. It is worth noting that compared with SnO₂ ETL substrate, the perovskite film based on SnO₂/GCC ETL exhibits the strongest (110) diffraction peak intensity at $q=1.01 \text{ \AA}^{-1}$, which will lead to better crystal orientation of the perovskite film and fully reflect the XRD spectrum results. Indicating that perovskite films grown on SnO₂/GCC ETL substrates have higher crystallinity.



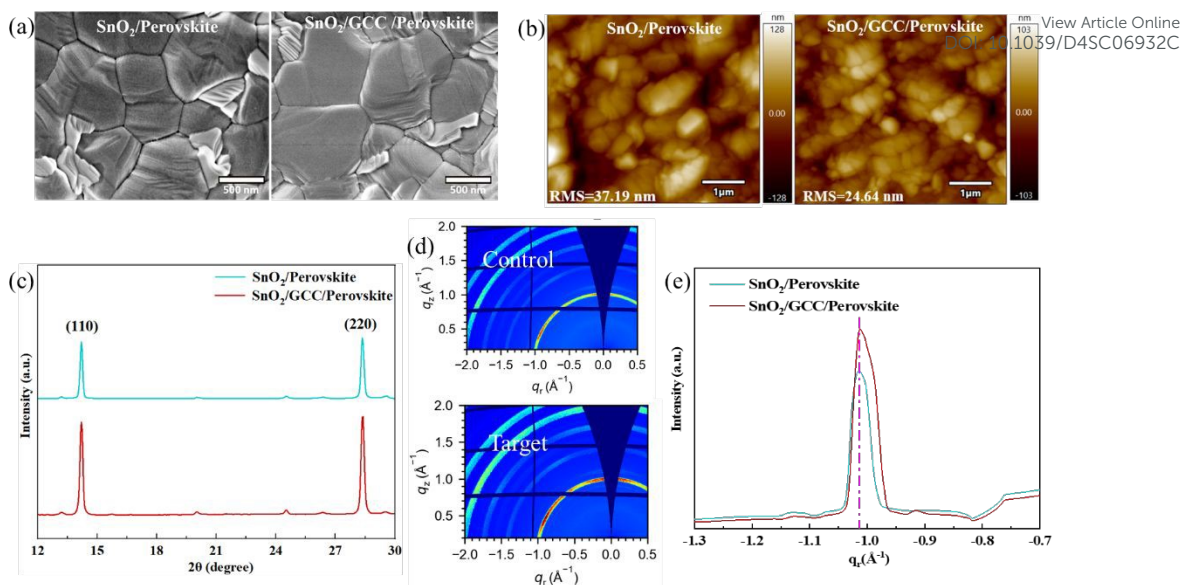


Fig. 4. (a) SEM and (b) AFM images of perovskite films deposited on SnO₂ and SnO₂/GCC ETLs. (c) XRD patterns of perovskite films. (d) 2D-GIWAXS images, and (e) Derived 1D integral analysis spectra of the perovskite films deposited on SnO₂ and SnO₂/GCC ETLs.

The optimized surface energy level and improved perovskite film quality will affect the dynamic transport and recombination of interface carriers. To further study the effect of GCC on the charge transfer and carrier extraction process of the perovskite layer, we characterized the steady-state photoluminescence (PL) spectra and time-resolved photoluminescence (TRPL) spectra of perovskite films on SnO₂ and SnO₂/GCC substrates, respectively. Fig. 5a shows the steady-state PL spectra of the perovskite layers on different substrates. The PL intensity indicates the carrier recombination rate of the perovskite film. For all thin film samples, the emitted light is incident from the side of the perovskite film. A strong PL peak at 796nm can be clearly observed in the perovskite film deposited on the original SnO₂ ETL. However, for the GCC modified samples, the intensity of the PL peak at the same position was significantly reduced. This result indicates that a more efficient electron extraction process occurred between SnO₂ and perovskite thin films, due to the strong chemical interactions between GCC and the perovskite and SnO₂ layers, which is consistent with the results of XPS. The Kelvin probe force microscope (KPFM) measurement is also used to visualize the surface potential of the SnO₂ film. The surface potential of the modified film (Fig. 5c) is significantly higher than that of the original (Fig. 5b),



indicating that the introduction of GCC can effectively modify the W_F of SnO₂ film. View Article Online
DOI: 10.1039/D4SC06932C

Fig. 5d shows the TRPL decay curves of perovskite layers on different substrates. The fitted values are listed in Table S2. This indicates that the introduction of GCC can promote the extraction and collection of charges at the interface, thereby increasing V_{OC} .

To verify the carrier transport capacity at the modified SnO₂/perovskite interface, we performed space charge limited current (SCLC) measurements. Fig. 5e shows the dark I-V curve of ITO/SnO₂(or SnO₂/GCC)/perovskite/[6,6]-phenyl-C61-butyric acid methyl ester (PCBM)/Ag pure electronic device. The curve is divided into the low-voltage region on the left and the trap-filling region on the right. At the same time, the voltage crossing point from the tangent of the ohmic region and the extension line of the trap-filling region is defined as the trap-filling limit voltage (V_{TFL}). The trap state density (N_t) of the carrier can be calculated by the following equation: ⁴³

$$N_t = \frac{2\varepsilon\varepsilon_0V_{TFL}}{qL^2}$$

where ε is the relative permittivity of the PVK material, ε_0 is the vacuum permittivity and q is the elemental charge. V_{TFL} is the trap-filling limiting voltage and L is the film thickness. The trap state density of the GCC-modified sample was calculated to be $1.15 \times 10^{16} \text{ cm}^{-3}$, which is significantly lower than the trap state concentration of the control device ($2.27 \times 10^{16} \text{ cm}^{-3}$). This is due to the effective defect passivation of GCC as an interface modifier and the improvement of the quality of perovskite films. In addition, Fig. 5f shows the dark J - V curves of two modified PSCs devices before and after modification, used to measure the dark current density of different devices to evaluate the characteristics of charge transfer. Compared with the basic device, the dark current density of PSCs devices optimized by GCC is significantly reduced. This indicates that GCC can passivate inherent defects at the interface, improve carrier transport efficiency, and suppress charge recombination at the SnO₂/perovskite interface, which verifies the results of the dark I - V curve.



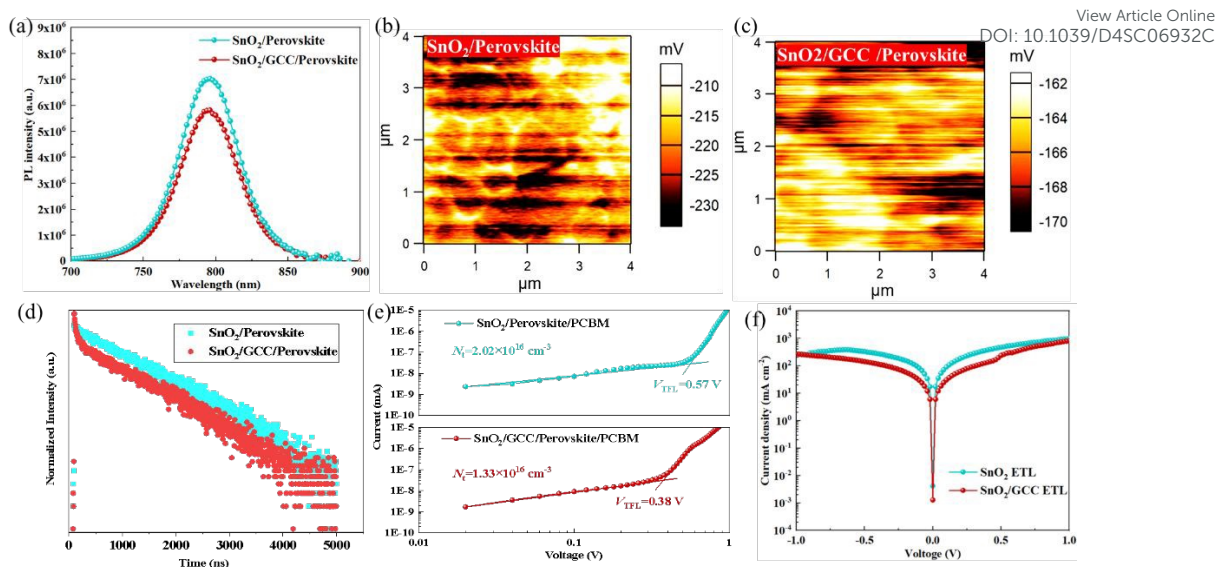


Fig. 5. (a) PL spectra of perovskite film deposited on ITO/SnO₂ and ITO/SnO₂/GCC. KPFM images of perovskite film deposited on (b) ITO/SnO₂ and (c) ITO/SnO₂/GCC. (d) TRPL spectra of perovskite film deposited on ITO/SnO₂ and ITO/SnO₂/GCC. (e) Dark $I-V$ curve of the electron-only device with ITO/SnO₂/perovskite/PCBM/Ag and ITO/SnO₂/GCC/perovskite/PCBM/Ag structures. (f) Dark $J-V$ curve of the devices with and without GCC treatment.

To study the effect of the GCC interface on the photovoltaic performance of the device, we measured the power output curves of PSCs with GCC modified SnO₂ under standard AM 1.5G illumination (Fig. 6a). It is worth noting that the GCC passivation layer plays a vital role in device performance. In detail, the control device based on pure SnO₂ ETL exhibits a champion PCE of 25.06% with a V_{OC} of 1.17 V, a J_{SC} of 25.59 mA cm⁻², and FF of 83.61%. Fig. 6b and Table S3 show the $J-V$ curves of PSCs devices with/without GCC modification measured by reverse scanning and forward scanning. The hysteresis phenomenon of PSCs is caused by the ion migration due to the high density of defect states in the perovskite material and the imbalance of charge transport inside the PSCs device. The hysteresis index (HI) is calculated by the equation:

$$HI = \frac{PCE_{RS} - PCE_{FS}}{PCE_{RS}}$$

Compared with the control device, the HI of the device after GCC modification is significantly reduced from 0.045 to 0.024, indicating that the device defects are reduced, which further illustrates the hysteresis elimination effect of GCC on PSCs at the interface. Fig. S7 shows the $I-V$ curves of devices based on SnO₂ and SnO₂/GCC ETLs.



From the results, it can be seen that after the introduction of the GCC interface, the performance of PSCs prepared based on the SnO₂/GCC ETL substrate was significantly enhanced under different scanning direction measurements. The external quantum efficiency (EQE) spectrum and integrated current of the device after GCC passivation are shown in Fig. 6c. The EQE measurement was performed to verify the reliability of J_{sc} . By integrating the EQE data on the entire measurement spectrum of the GCC-modified device, the integrated J_{sc} was calculated to be 25.59 mA cm⁻², which was close to the value extracted from the $J-V$ curve. The long-term stability of PSCs is the most important factor affecting their commercialization, so we finally studied the effect of GCC modification on the stability of PSCs. The steady-state power output is shown in Fig. 6d, the stable output PCE of GCC-modified PSC after 300 s is 24.50%, indicating that GCC-modified PSCs can maintain stable output capability. Additionally, Fig. S9 shows the contact angle measurements of different ETLs. Fig. S10 shows the change in contact GCC angle of perovskite film before and after modification. The contact angle of perovskite precursor based on GCC-modified SnO₂ film increases from 43° to 59°. This is due to the reaction between the carboxyl groups unique to GCC and the free hydroxyl defects on the surface of SnO₂, which enhances the hydrophobicity of the perovskite film. Finally, we evaluated the environmental stability of unencapsulated PSCs. Additionally, the GCC-modified device exhibited a higher recombination resistance, as shown in Fig. S11, which is beneficial for reducing carrier recombination and improving charge transport. Fig. S12 shows the statistical distribution of photovoltaic parameters for devices manufactured using SnO₂ and SnO₂/GCC. As shown in Fig. 6e, after continuously placing the control device and GCC-modified PSCs in ambient air for 1080 hours, the control device only retained 70% of its original PCE, while the GCC-modified device retained 91% of its original PCE. This good stability can be attributed to the high crystallinity of perovskite grains and the defect passivation of GCC between SnO₂ and perovskite layers. These results strongly indicate that introducing GCC molecular bridges at the buried interface can reduce the risk of device degradation caused by external factors. As shown in Fig. S13, the GCC modified device exhibits significantly enhanced long-term stability.



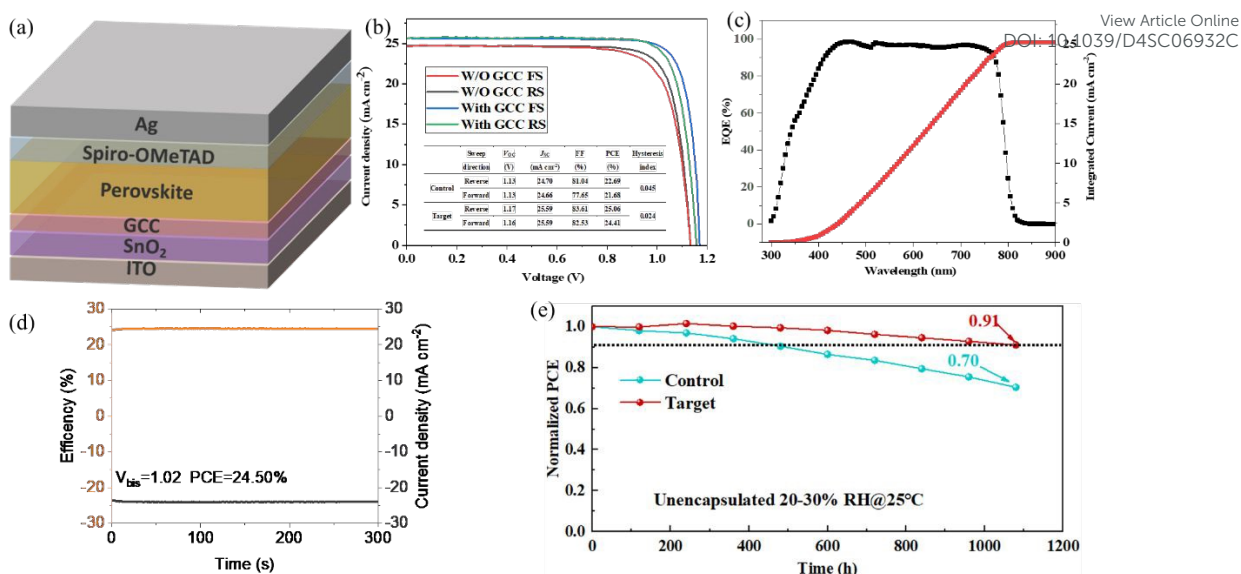


Fig. 6. (a) Schematic illustration of an implemented PSCs. (b) J - V curves of PSCs device with and without GCC treatments. (c) The EQE spectrum and integrated current of the PSCs device after GCC passivation. (d) steady-state power output curves of PSCs. The environmental stability curves of the control and GCC-modified unencapsulated devices under 20-30% RH@25°C.

3. Conclusion

In summary, we have successfully demonstrated that GCC acts as a bidirectional cross-linking agent between SnO₂ ETL and the perovskite layer to simultaneously accelerate the extraction and transport of electrons at the buried interface and improve the crystal growth of perovskite films. Highly efficient and stable PSCs are achieved by interface energy level alignment and defect passivation. Finally, the high PCE of 25.06% can be achieved. In addition, after continuously placing the unencapsulated control group and GCC modified PSCs in ambient air (20-30% RH at 25°C) for 1080 hours, the control group only retained 70% of its original PCE, while the GCC modified device retained 91% of its original PCE. It exhibits excellent operational stability. Our strategy provides a simple and efficient and stable PSCs, thereby promoting the large-scale commercial application of PSCs.

4. Experimental section

4.1 Materials



GCC was synthesised according to the previous published paper as follows. Chlorobenzene (CB), anisole, isopropanol (IPA), N, N-dimethylformamide (DMF), and dimethyl sulfoxide (DMSO) were purchased from Sigma-Aldrich. Lead iodide (PbI₂) and cesium iodide (CsI) were obtained from Xi'an Polymer Light Technology Corp. Formamidinium iodide (FAI), methylammonium chloride (MACl) and lead methyl bromide (MAPbBr₃) were purchased from Great Cell. Spiro-OMeTAD, 4-tert-butylpyridine (tBP) and lithium bis(trifluoromethanesulphonyl)imide (Li-TFSI) were purchased from Advanced Election Technology Co., Ltd.

4.2 Device preparation

ITO (1.5cm × 1.5cm) was washed with deionized water containing detergent, ethanol, and isopropanol under ultrasonic treatment. The washing time is 15 min. After that, N₂ is used for drying treatment, and then ultraviolet ozone is used for treatment. The treatment time is 40 min, resulting in a hydrophilic surface. The SnO₂ solution was spin-coated on the ITO substrate at 4000 rpm, the time was 30 s, and then the annealing treatment was carried out under the condition of ambient air at 150°C, and the annealing time was 30min. When the device is processed by the GCC, the GCC solution is first spin-coated on the top of the ITO/SnO₂ substrate, then rotated at a speed of 5000 rpm, the rotation time is 30 s, and then the perovskite layer is spin-coated. The sample was annealed at 100°C in ambient air, and the annealing time was 5 min. After annealing, the device is moved into the glove box, and the perovskite film is prepared by a one-step anti-solvent spin coating method. To prepare a perovskite precursor solution, dissolve PbI₂ (705.33mg), FAI (233.54mg), MAPbBr₃ (18.20mg), MACl (33.67mg) and CsI (10.91mg) in a mixed solution of 1 mL DMF/DMSO (9:1). The prepared perovskite precursor solution was spin-coated on the SnO₂ film at a speed of 1000 rpm, and the spin-coating time was 10 s. After that, 300 μL of Anisole was used to inject the SnO₂ film at a speed of 4000 r/min for 20 s. Then, remove the device from the glove box and anneal it in ambient air at 100 °C, The annealing time is 40 min. After annealing, put the device into the glove box again and spin-coat the HTL layer. Spiro-OMeTAD powder, tBP and Li-TFSI solution were added to CB, and then the Spiro HTL solution was spin-coated on the perovskite film at a rate of 3000 rpm for 30 s. And oxidized in air, the oxidation time is 18 h. Finally, under high vacuum (<3.0 × 10⁻⁴ Pa), heat and evaporate 100 nm of silver as the electrode.



4.3 Characterizations

View Article Online
DOI: 10.1039/D4SC06932C

J-V scans were performed with a Keithley 2400 Source Meter under simulated AM 1.5G illumination at one sun (100 mW cm^{-2}) using a solar simulator (EnliTech SS-F5-3A), and light intensities were calibrated using a silicon reference solar cell. The measurements were taken in a glove box with a concentration of less than 0.1 ppm of oxygen and water. The devices were tested in reverse scan ($1.2 \text{ V} \rightarrow -0.2 \text{ V}$, step 0.02 V) and forward scan ($-0.2 \text{ V} \rightarrow 1.2 \text{ V}$, step 0.02 V). For the stability test, the devices were stored under indoor light illumination. The EQE spectrum was measured at room temperature in the air with a QTEST HIFINITY 5 (Crowntech Inc., USA). The light intensity was calibrated using a standard single-crystal Si photovoltaic cell. The SEM measurements were performed using a Hitachi S4800 electron microscope. The XRD patterns were analyzed using a Rigaku-D/Max-3A X-ray diffractometer with monochromatic Cu K α irradiation ($\lambda = 1.5406 \text{ \AA}$). The GIWAXS measurements were performed at the BL14B1 beamline of the Shanghai Synchrotron Radiation Facility (SSRF) with an X-ray wavelength of 1.24 \AA . The X-ray beam size was approximately $0.2 \times 0.3 \text{ mm}^2$, characterized by horizontal and vertical slits. The UV/Vis transmittance spectrum was measured with a UV/Vis spectrophotometer (U-3900H, Hitachi High-tech Co., Ltd). The TRPL and PL measurements were performed on the FLS1000. The XPS and UPS measurements were performed using a Kratos Axis Supra photoelectron spectrometer with a monochromatic source of Al (K α) (1,486.6 eV) X-rays. The AFM and KPFM images were captured using an atomic force microscope in Dimension Icon.

Conflicts of interest

The authors declare no competing financial interests.

Acknowledgments

This work was financially supported by the Doctoral research start-up project of Xi'an Polytechnic University (107020579), Shaanxi Natural Science Foundation of China (2023-JC-QN-0680), the National Natural Science Foundation of China (52402055), the Science and Technology Plan Project of Xi'an City (23GXFW0015), National Natural Science Foundation of China (52203125), Innovation Capability Support



Program of Shaanxi (2024ZC-KJXX-044), Taishan Industrial Experts Programme
(tscx202312119).

[View Article Online](#)

DOI: 10.1039/D4SC06932C



References

1. H. Lu, Y. Liu, P. Ahlawat, A. Mishra, W. R. Tress, F. T. Eickemeyer, Y. Yang, F. Fu, Z. Wang, C. E. Avalos, B. I. Carlsen, A. Agarwalla, X. Zhang, X. Li, Y. Zhan, S. M. Zakeeruddin, L. Emsley, U. Rothlisberger, L. Zheng, A. Hagfeldt and M. Grätzel, *Science*, 2020, **370**.
2. J. H. Noh, S. H. Im, J. H. Heo, T. N. Mandal and S. I. Seok, *Nano Lett.*, 2013, **13**, 1764-1769.
3. D. P. McMeekin, G. Sadoughi, W. Rehman, G. E. Eperon, M. Saliba, M. T. Hörantner, A. Haghighirad, N. Sakai, L. Korte, B. Rech, M. B. Johnston, L. M. Herz and H. J. Snaith, *Science*, 2016, **351**, 151-155.
4. S. D. Stranks, G. E. Eperon, G. Grancini, C. Menelaou, M. J. Alcocer, T. Leijtens, L. M. Herz, A. Petrozza and H. J. Snaith, *Science*, 2013, **342**, 341-344.
5. W. J. Yin, T. Shi and Y. Yan, *Adv. Mater.*, 2014, **26**, 4653-4658.
6. K. He, J. Zhang, X. Zhao, F. Liu, R. Chen, J. Ma, B. Du, Y. Wang and L. Song, *J. Mater. Chem. A*, 2024, **12**, 19310-19320.
7. G. Wang, L. Liao, L. Niu, L. Chen, W. Li, C. Xu, E. Mbeng, Y. Yao, D. Liu and Q. Song, *Nanoscale*, 2019, **11**, 12108-12115.
8. Q. Cao, T. Wang, X. Pu, X. He, M. Xiao, H. Chen, L. Zhuang, Q. Wei, H.-L. Loi, P. Guo, B. Kang, G. Feng, J. Zhuang, G. Feng, X. Li and F. Yan, *Adv. Mater.*, 2024, **36**, 2311970.
9. C. Zuo, L. Tan, H. Dong, J. Chen, F. Hao, C. Yi and L. Ding, *DeCarbon*, 2023, **2**, 100020.
10. X. Zhu, M. Du, J. Feng, H. Wang, Z. Xu, L. Wang, S. Zuo, C. Wang, Z. Wang, C. Zhang, X. Ren, S. Priya, D. Yang and S. F. Liu, *Angew. Chem. Int. Ed.*, 2021, **60**, 4238-4244.
11. J. Ma, L. Wang, K. He, Y. Sun, B. Li, Q. Zhao and B. Du, *J. Mater. Chem. C*, 2024, **12**, 10837-10856.
12. J. Zhang, W. Li, X. Lv, Y. Ji, W. Huang, T. Bu, Z. Ren, C. Yao, F. Huang, Y.-B. Cheng and J. Tong, *Sol. RRL*, 2024, **8**, 2400184.
13. D. B. Khadka, Y. Shirai, M. Yanagida, H. Ota, A. Lyalin, T. Taketsugu and K. Miyano, *Nat. Commun.*, 2024, **15**, 882.
14. Z.-R. Lan, Y.-D. Wang, J.-Y. Shao, D.-X. Ma, Z. Liu, D. Li, Y. Hou, J. Yao and Y.-W. Zhong, *Adv. Funct. Mater.*, 2024, **34**, 2312426.
15. X. Kong, Z. Li, Y. Jiang, Z. Xu, S.-P. Feng, G. Zhou, J.-M. Liu and J. Gao, *Surf. Interfaces*, 2021, **25**, 101163.
16. J. Zhuang, P. Mao, Y. Luan, N. Chen, X. Cao, G. Niu, F. Jia, F. Wang, S. Cao and J. Wang, *Adv. Funct. Mater.*, 2021, **31**, 2010385.
17. Y. Zhang, L. Xu, Y. Wu, Q. Zhou, Z. Shi, X. Zhuang, B. Liu, B. Dong, X. Bai, W. Xu, D. Zhou and H. Song, *Nano Energy*, 2021, **90**, 106610.
18. H. Min, D. Y. Lee, J. Kim, G. Kim, K. S. Lee, J. Kim, M. J. Paik, Y. K. Kim, K. S. Kim, M. G. Kim, T. J. Shin and S. Il Seok, *Nature*, 2021, **598**, 444-450.
19. J. Zhang, B. Yu, Y. Sun and H. Yu, *Adv. Energy Mater.*, 2023, **13**, 2300382.
20. J. Park, J. Kim, H.-S. Yun, M. J. Paik, E. Noh, H. J. Mun, M. G. Kim, T. J. Shin and S. I. Seok, *Nature*, 2023, **616**, 724-730.
21. J. Wang, S. Luo, X. Tang, S. Xiao, Z. Chen, S. Pang, L. Zhang, Y. Lin, J. He and Y. Yuan, *ACS Energy Lett.*, 2021, **6**, 3634-3642.
22. T. Wu, L. K. Ono, R. Yoshioka, C. Ding, C. Zhang, S. Mariotti, J. Zhang, K. Mitrofanov, X. Liu, H. Segawa, R. Kabe, L. Han and Y. Qi, *Energy Environ. Sci.*, 2022, **15**, 4612-4624.



23. K. Wei, L. Yang, J. Deng, Z. Luo, X. Zhang and J. Zhang, *ACS Appl. Energy Mater.*, 2022, **5**, 7458. View Article Online
DOI: 10.1039/D4SC06932C
7465.
24. J. Chen and N.-G. Park, *ACS Energy Lett.*, 2020, **5**, 2742-2786.
25. Z.-W. Gao, Y. Wang and W. C. H. Choy, *Adv. Energy Mater.*, 2022, **12**, 2104030.
26. J. Chen, X. Zhao, S.-G. Kim and N.-G. Park, *Adv. Mater.*, 2019, **31**, 1902902.
27. Q. Jiang, Y. Zhao, X. Zhang, X. Yang, Y. Chen, Z. Chu, Q. Ye, X. Li, Z. Yin and J. You, *Nat. Photonics*, 2019, **13**, 460-466.
28. Y. Zhao, F. Ma, Z. Qu, S. Yu, T. Shen, H.-X. Deng, X. Chu, X. Peng, Y. Yuan, X. Zhang and J. You, *Science*, 2022, **377**, 531-534.
29. X. Liang, M. Singh, F. Wang, P. W. K. Fong, Z. Ren, X. Zhou, X. Wan, C. M. Sutter-Fella, Y. Shi, H. Lin, Q. Zhu, G. Li and H. Hu, *Advanced Science*, 2024, **11**, 2305572.
30. Q. Zhuang, C. Zhang, C. Gong, H. Li, H. Li, Z. Zhang, H. Yang, J. Chen and Z. Zang, *Nano Energy*, 2022, **102**, 107747.
31. J. Chen and W. C. H. Choy, *Sol. RRL*, 2020, **4**, 2000408.
32. X. Ji, L. Bi, Q. Fu, B. Li, J. Wang, S. Y. Jeong, K. Feng, S. Ma, Q. Liao, F. R. Lin, H. Y. Woo, L. Lu, A. K. Y. Jen and X. Guo, *Adv. Mater.*, 2023, **35**, 2303665.
33. S. Zhang, M. Li, H. Zeng, X. Zheng, L. Luo, S. You, Y. Zhao, R. Liu, C. Tian and X. Li, *ACS Energy Lett.*, 2022, **7**, 3958-3966.
34. Y. Zhang, T. Kong, H. Xie, J. Song, Y. Li, Y. Ai, Y. Han and D. Bi, *ACS Energy Lett.*, 2022, **7**, 929-938.
35. C. Wang, J. Wu, S. Wang, Z. Yan, X. Liu, G. Li, L. Chen, S. Zhu, W. Sun and Z. Lan, *Sol. RRL*, 2022, **6**, 2100995.
36. Z. Zhang, B. Zhang, N. Grishkewich, R. Berry and K. C. Tam, *Adv. Sustain. Syst.*, 2019, **3**, 1800156.
37. X. Li, W. Sheng, X. Duan, Z. Lin, J. Yang, L. Tan and Y. Chen, *ACS Appl. Mater. Interfaces*, 2022, **14**, 34161-34170.
38. L. Yang, M. Wu, F. Cai, P. Wang, R. S. Gurney, D. Liu, J. Xia and T. Wang, *J. Mater. Chem. A*, 2018, **6**, 10379-10387.
39. X. Zuo, B. Kim, B. Liu, D. He, L. Bai, W. Wang, C. Xu, Q. Song, C. Jia, Z. Zang, D. Lee, X. Li and J. Chen, *Chemical Engineering Journal*, 2022, **431**, 133209.
40. L. Yin, C. Ding, C. Liu, C. Zhao, W. Zha, I. Z. Mitrovic, E. G. Lim, Y. Han, X. Gao, L. Zhang, H. Wang, Y. Li, S. Wilken, R. Österbacka, H. Lin, C.-Q. Ma and C. Zhao, *Adv. Energy Mater.*, 2023, **13**, 2301161.
41. J.-W. Lee, H.-S. Kim and N.-G. Park, *Acc. Chem. Res.*, 2016, **49**, 311-319.
42. W. Hui, X. Kang, B. Wang, D. Li, Z. Su, Y. Bao, L. Gu, B. Zhang, X. Gao, L. Song and W. Huang, *Nano Lett.*, 2023, **23**, 2195-2202.
43. Z. Wang, Y. Lu, Z. Xu, J. Hu, Y. Chen, C. Zhang, Y. Wang, F. Guo and Y. Mai, *Advanced Science*, 2021, **8**, 2101856.



The data supporting this article have been included as part of the Supplementary Information. [View Article Online](#)
DOI: 10.1039/D4SC06932C

Open Access Article. Published on 18 December 2024. Downloaded on 12/19/2024 9:47:34 AM.
This article is licensed under a Creative Commons Attribution-NonCommercial 3.0 Unported Licence.

